Mapping changes in uterine contractility during the ovulatory cycle with wide-area calcium imaging in live mice.

David J. Combs[1,2], Eric M. Moult[2], Sarah K. England[3], Adam E. Cohen[2,4*]

[1]Department of Anesthesiology, Perioperative and Pain Medicine, Brigham and Women's Hospital, Harvard Medical School
[2]Department of Chemistry and Chemical Biology, Harvard University
[3]Department of Obstetrics and Gynecology, Center for Reproductive Health Sciences, Washington University School of Medicine
[4]Department of Physics, Harvard University

[*]cohen@chemistry.harvard.edu

Abstract

Uterine contraction patterns vary during the ovulatory cycle and during gestation, but prior measurements have produced limited and conflicting information on these patterns. We combined a virally delivered genetically encoded calcium reporter (GCaMP8m) and ultra-widefield imaging in live nonpregnant mice, and characterized uterine calcium dynamics at organ-scale throughout the estrus cycle. At all stages, activity emanated from multiple loci of initiation (LOIs) and had irregular patterns in time. The average frequency of calcium events varied strongly with cycle stage, being lowest in proestrus (0.01 ± 0.02 Hz) and estrus (0.02 ± 0.01 Hz), higher in metestrus (0.09 ± 0.02 Hz), and highest in diestrus (0.16 ± 0.04 Hz; means ± s.e.m., $p < 7 \times 10^{-6}$). In proestrus and metestrus, the LOIs showed a strong preference for the rostral end of the uterine horn (82% and 74% of events, respectively), whereas LOIs in metestrus and diestrus were multifocal and evenly distributed across the horn, with propagation equally likely in the rostral and caudal directions. Event velocities in proestrus (1.6 ± 1.2 mm/s) and estrus (1.6 ± 1.0 mm/s) were faster than in metestrus (0.13 ± 0.01 mm/s) and diestrus (0.13 ± 0.02 mm/s). These results establish that uterine activity rises following ovulation, peaking in diestrus, and that there is no anatomically fixed uterine pacemaker, although the ovarian end of the uterus exhibits pacer-like properties in proestrus and estrus.

Introduction

Uterine contractions support important biological functions. In pregnancy, they are central to labor and delivery, as well as postpartum hemostasis (Malik et al., 2021). Aberrant uterine contractility is implicated in preterm birth, dystocia, postpartum hemorrhage, infertility, dysmenorrhea, and endometriosis, all common conditions, many of which carry significant morbidity or mortality. In non-pregnancy, uterine contractions may assist in fertilization, implantation and the clearance of menstrual debris (Aguilar and Mitchell, 2010).

Cellular and molecular studies have identified many of the ion channels and other proteins central to uterine myocyte electrophysiology (Wray and Arrowsmith, 2021). However, it is not clear how these components produce tissue-scale activity, and how that activity is coordinated and controlled during ovulation and pregnancy. As contractions in pregnancy are quasi-periodic (Lammers, 2013) and contractions in non-pregnancy vary in frequency and origin with the ovulatory cycle (Talo and Kärki, 1976; Ishikawa and Fuchs, 1978; Crane and Martin, 1991; Griffiths et al., 2006; Wray and Noble, 2008; Dodds et al., 2015; Ma et al., 2020), prior work sought evidence for uterine pacemakers (Young, 2018). However, without high-quality organ-scale maps of uterine activity patterns, the search for a putative uterine pacemaker is difficult. Past searches have largely assumed similarity to known pacing systems (*e.g.* heart or gut) and looked for analogous electrical activity or histologic features (Duquette et al., 2005; Lutton et al., 2018), yielding conflicting views. High resolution activity maps in live animals could pinpoint the loci driving organ-wide activity and could inform future searches for coordinating mechanisms.

Measurement of calcium dynamics with genetically encoded calcium indicators presents a solution to this challenge. These tools are readily deployed at organ scale in living animals and have been used in brain (Ren and Komiyama, 2021), mammary ducts (Stevenson et al., 2020), skeletal muscle (Sanchez et al., 2021), and heart (Hou et al., 2014; Jia et al., 2023). In combination with cell type-specific drivers, these indicators can report on the activity of cellular subpopulations within a complex tissue.

Here, we use the genetically encoded calcium indicator jGCaMP8m to map myometrial calcium dynamics across an entire uterine horn in live mice at different stages of the estrous cycle. These measurements clarified the nature of cycle-dependent changes in propagation velocity, locus of initiation, and the event rate. We also identified a dominant locus of initiation for excitation events in the ovarian end of the uterine horn, but it was aperiodic and active only before and during ovulation (proestrus and estrus) and not afterward (metestrus and diestrus).

Results

Adeno-associated virus injection enables in vivo myometrial transgene expression

To look for evidence of uterine pacemaking, we developed methods for *in vivo* transgene delivery and calcium imaging. Adeno-associated virus (AAV)-mediated transgene expression has not been reported in uterine smooth muscle. Plasmid-based uterine muscle-specific promoters have not been described, and no transgenic mice have been created that express site-specific recombinases exclusively in uterine smooth muscle. We therefore chose a commercially available AAV with payload comprising the universal CAG promoter and Cre-dependent expression of the calcium indicator jGCaMP8m (Zhang et al., 2023). We chose the AAV9 capsid serotype, which has been successfully used for *in vivo* transgene expression in skeletal and cardiac muscle (Weinmann et al., 2020). We used progesterone-receptor (PR)-Cre mice to target expression to myometrium (Yang et al., 2013). Virus was injected into the anterior face of the uterine horn along its longitudinal axis via an open abdominal surgery (Figure 1; Methods). In virus-injected animals, estrous staging was determined by vaginal cytology (Figure 1, Supplemental Figure 1; Methods).

Virus injection led to expression of jGCaMP8m in the injected, but not the contralateral, uterine horn (Supplemental Figure 2). Despite injections only in the anterior face of the uterine

horn, jGCaMP8m expression spread around the circumference of the organ. jGCaMP8m expressed in both circular and longitudinal muscle layers (Supplemental Figure 2). Consistent with the known tissue-specific expression pattern of Cre in PR-Cre mice (Soyal et al., 2005), jGCaMP8m also expressed in the endometrium. Expression lasted for at least 12 weeks after injection. Injected uteri appeared anatomically normal (Supplemental Figure 3). Virus injection and transgene expression did not produce detectable adverse impacts on reproduction, as pregnancy in virus-injected animals was readily achieved (n = 9) in the same time frame (< 3 months post injection) as our imaging experiments.

We also tried crossing two Cre driver lines (PR-Cre and AMHR2-Cre) with a Cre-dependent GCaMP6s reporter mouse line to drive whole-uterus reporter expression. Female offspring expressed calcium indicator throughout their uteruses, but these animals had atrophic uteri and were infertile, so this strategy was not pursued further (Supplemental Figure 4 and Supplemental Materials). Attempts to deliver transgenes by direct electroporation into wild-type uteruses were also not successful.

In addition to live animal imaging (see below), we tried imaging whole-uterus explants, but despite an extensive search of conditions, we found that the explanted uteri always showed markedly less spontaneous activity than *in vivo*. Mechanical or electrical stimuli could evoke activity in the explants, confirming that the tissue was alive (Supplemental Figure 5 and Supplemental Materials).

Wide-area live animal calcium imaging reveals estrous-related changes in calcium dynamics

We imaged uterine calcium dynamics *in vivo* in mice expressing virally delivered jGCaMP8M (Figure 1B-E, Supplemental Movies 1-4). We observed different kinds of events. Some excitations comprised elevated calcium in rings around the tissue, coupled with a local reduction in organ diameter (Figure 1B, 1D). Other excitations increased calcium in axially elongated strips, coupled with long axis shortening (Figure 1C,1E). We propose that these different events reflect independent activation of the circular and longitudinal muscle layers, respectively. In no estrous stage did activity appear to arise exclusively in one muscle layer (see Discussion). Fluorescence dynamics in the injected horn were much larger than the small motion-associated changes in tissue autofluorescence from the contralateral horn (Supplemental Figure 6).

Recordings of calcium dynamics were taken from mice in all four estrous stages (n = 5 mice per stage). Qualitatively, videos from proestrus and estrus mice had markedly less activity than those from metestrus and diestrus mice (Supplemental Movies 1-4). To analyze differences in activity among the four estrous stages, we developed an image processing pipeline to extract and quantify uterine excitation events (Supplemental Figure 7, Supplemental Materials). In brief, we used motion-tracking and non-rigid deformation algorithms to undo the effects of tissue motion. We then defined a piecewise linear contour along the axis of the expressing uterine horn, and projected the fluorescence dynamics onto this axis, leading to fluorescence kymographs comprising one time dimension and one spatial dimension along the uterine axis (Figure 2A). This procedure discarded information about circumferential calcium dynamics, but visual inspection of the movies showed that most of the propagation was axial, both for activation of the longitudinal and circumferential muscle layers. We then used a combination of machine learning-based (Jakobs et al., 2019) and feature-based algorithms to identify calcium events and to quantify their locus of initiation, propagation speed, propagation duration, full-width at half maximum, (Figure 2, Figure 3, Methods).

We compared the properties of calcium events across estrous stages. Propagation velocities in proestrus (2.3 $\pm$ 1.1 mm/s, median ± s.d.) and estrus (1.2 $\pm$ 0.9 mm/s) were faster than in metestrus (0.13 $\pm$ 0.01 mm/s) and diestrus (0.12 $\pm$ 0.02 mm/s; $p < 0.01$, 1 way ANOVA , Figure 2B). Median event propagation distances (as magnitudes) in proestrus and estrus appeared slightly higher than in metestrus and diestrus, but this did not achieve statistical

significance (Figure 2C). To look at the duration of events at a given location (*i.e.* at a particular kymograph spatial coordinate), event-triggered averages were generated from their leading half maxima. Full widths at half maximum (FWHM), a measure of the duration of calcium elevation at a given location, of these mean event traces did not differ by estrous stage (Figure 2D). Event rates (number of events/total recording time, Figure 3A) were much lower for proestrus (0.01 ± 0.004 Hz) and estrus (0.009 ± 0.01 Hz) than for metestrus (0.09 ± 0.02 Hz) and diestrus (0.17 ± 0.05 Hz; $p < 1x10^{-6}$).

A region with pacer-like features exists in proestrus and estrus, but not metestrus and diestrus

In the heart, an anatomically and molecularly distinct pacemaker region coordinates the beating of the whole organ. Whether an analogous structure exists in the uterus has been controversial (Lammers, 2013; Young, 2018). We searched for pacemaker-like dynamics in the uterine Ca^{2+} signal. Two key elements of a pacing system are localization and periodicity. That is, events may originate from a single locus or from multiple loci; and may occur periodically or at irregular intervals.

To examine where events initiated, we mapped our data onto a normalized uterine horn longitudinal axis, and then sorted event LOIs into deciles along this axis. During estrus and proestrus, activity primarily initiated from regions near the oviduct, with 82% and 74% of events, respectively, emerging from two deciles closest to the oviduct (Figure 3B). In contrast, events in metestrus and diestrus showed an even distribution of LOIs across the uterine horn (Figure 3B). The spatially distributed LOIs in diestrus and metestrus appeared equally likely to propagate toward the oviduct or toward the cervix, whereas those in proestrus and estrus showed a strong directional bias to propagate in the cervical direction (Figure 3C).

Although portions of some kymographs showed periodic activity emanating from a particular locus, this periodicity did not appear stable. To examine the temporal structure of events, we generated power spectra from kymographs of recordings at each estrous stage (Figure 4). The power spectra of dynamics in the uterine horn did not have any peaks, indicating absence of periodicity at any estrous stage. This observation was consistent with the wide distribution of inter-event-intervals for all four estrous stages (Figure 3D). To confirm that we could detect a periodic signal, we examined the oviduct, which, in a subset of samples, exhibited jGCaMP8m signal, likely acquired from viral injections into the oviductal end of the uterine horn. Consistent with previous reports of myosalpinx contractions in the oviduct paced by interstitial cells of Cajal (Dixon et al., 2019), the oviductal calcium signal was highly periodic with a typical frequency of 0.15 Hz (Figure 4). We did not observe sustained synchrony of oviductal and uterine activity in any estrus stage.

Discussion

We developed an approach for live animal organ-scale imaging of uterine calcium activity and mapped changing activity patterns throughout the mouse ovulatory cycle. Prior to ovulation (proestrus and estrus) a region near the oviductal end of the uterus is the dominant locus of initiation for uterine excitations, but after ovulation (metestrus and diestrus), excitations start at loci homogeneously distributed throughout the organ. The primary effect of the cycle on contractility is a marked increase of activity following ovulation, peaking in diestrus.

Prior descriptions of live animal uterine imaging exist for detecting fluorescently labeled immune cells (Zenclussen et al., 2013) and for performing contractility analysis from videos of organ motion (Crane and Martin, 1991; Zhang et al., 2019). However, these approaches impose significant uterine stretch, likely altering endogenous dynamics (Young, 2016), and/or view only a segment of the uterine horn.

Several electromyogram (EMG) studies in live animals show drops in activity rates from estrus to diestrus (Ruckebusch and Bayard, 1975; Talo and Kärki, 1976; Downing et al., 1981;

Wheaton et al., 1988; Ishikawa and Fuchs, 1978). Ishikawa and Fuchs combined EMG with intrauterine pressure (IUP) measurements, revealing that IUP depends not just on the rate but also the duration of electrical activity, which was longest in diestrus. They also found fastest propagation in proestrus and estrus and that activity originated near the cervical end in proestrus and near the ovarian end in diestrus. In contrast, a later motion and EMG analysis of the cervical end of rat uteri *in situ* showed propagation toward the cervix predominating at all stages (Crane and Martin, 1991). Studies of tension, or tension and calcium, in rodent myometrial strips differ on which phases are most active (Griffiths et al., 2006; Wray and Noble, 2008). Tension measurements on explants from mice showed a dominant oviductal site in all stages except metestrus, slower propagation speeds in estrus and diestrus than in proestrus and metestrus, and diestrus as the most quiescent phase (Dodds et al., 2015). In dissected sheets of mouse longitudinal muscle, estrous samples had firing that was shorter, higher frequency, lower amplitude, and more synchronous than non-estrous samples (Ma et al., 2020), perhaps indicative of rapid but weak electrical activity during estrous.

Dissected preparations, whether small strips or larger pieces, necessarily involve cutting across uterine muscle fibers, creating damage that may result in aberrant electrical activity. Even without dissection, explanted organs may be deprived of circulating factors or paracrine or neural stimuli. Our whole organ explants did not reproduce live animal uterine physiology. While *in vivo* IUP and EMG measurements lack these problems, the former suffers from poor spatial and temporal resolution, and the latter from poor spatial resolution. These factors may explain the inconsistent results of the above studies, and speak to the advantage of our approach. Nearly all of these studies also identified estrus as the most active stage, the opposite of what we report here. This may be due to the above limitations of these approaches or perhaps because cavity pressure measurements and small numbers of sharp electrodes are not equally sensitive to activity in the two muscle layers.

Higher propagation velocities but lower event rates in proestrus and estrus are consistent with increases in gap junction expression in those phases (Thilander et al., 1993), enhancing coupling and speeding electrical conduction but also increasing electrotonic loading of putative initiation sites (Sheldon et al., 2015). Differences in event rates may also be explained by the known and antagonistic effects of progesterone and 17β-estradiol on L type calcium channel expression, leading to higher calcium channel current densities in diestrus (Rendt et al., 1992). Similarly, compared to diestrus, potassium channel subtypes with faster activation kinetics predominate in estrus, which would shorten action potential and burst durations (Toro et al., 1990). The circular and longitudinal layers of the rodent myometrium have different activity (Kawarabayashi and Osa, 1976; Chamley and Parkington, 1984). We did not attempt to sort our calcium events by layer, but videos of dynamics suggested that activity in metestrus and diestrus was mostly from the circular layer while in proestrus and estrus, longitudinal layer events occurred too, though still less frequently than circular layer events. Longitudinal layer events also had faster propagation along the organ long axis at all stages. Cycle-dependent shifts in activity between these two muscle layers may also partially explain the changes we observed in overall activity patterns.

The physiological basis of the shift toward ovarian-end initiation during proestrus and estrus is not known. Single cell transcriptomic analysis of juvenile and adult mouse uteri identified four myocyte subtypes (Mucenski et al., 2019). Studies of uterine pacemakers in estrous should compare the gene expression patterns and electrophysiology of the ovarian end to the bulk horn, during epochs of localized vs. delocalized event initiation. .

Activity in the non-pregnant myometrium is suggested to facilitate sperm transport, blastocyst implantation, and the clearance of menstrual debris (Aguilar and Mitchell, 2010). While mice, like most mammals, do not menstruate, proliferating endometrial tissues begin to degenerate and are ultimately resorbed in diestrus (Bertolin and Murphy, 2014). We speculate that vigorous bidirectionally propagating activity in metestrus and diestrus may assist endometrial

breakdown. Dynamics at 3-4 days post-coitus, when the blastocyst enters the horn (Wang and Dey, 2006), may be different from those of estrous.

Unlike mice, women menstruate, have ~28 day cycles, and have unicornuate uteri without distinct circular and longitudinal muscle layers (Aguilar and Mitchell, 2010). However, analogously to the rodent estrous cycle, human myometrial activity varies over the menstrual cycle, with the strongest (and most painful) activity occurring at menstruation (Bulletti et al., 2004). The molecular mechanisms that augment myometrial activity following ovulation could be common to both species. However, perhaps because it is periodic, most studies of human non-pregnant myometrial activity have focused on the peristaltic activity of the thin layer of subendometrial muscle which is most active in estrous (Kunz and Leyendecker, 2002; Wang et al., 2023). It is unclear whether mice have a similar layer, although in principle, subendometrial activity and mouse estrus activity could share hormonally sensitive activating mechanisms. In any case, our study emphasizes the seemingly overlooked activity of bulk uterine muscle during endometrial decline, which in humans is connected to dysmenorrhea and endometriosis, common debilitating conditions.

In conclusion, we have developed a technique for expressing transgenes in the myometrium and for live animal imaging of uterine excitation dynamics at tissue-scale. We show that, in contrast to prior reports, uterine activity rises following ovulation, peaking in diestrus. Proestrus and estrus stages feature rare, fast-propagating activity whose initiation is localized near ovarian end of the organ. This area could house a transiently present non-periodic pacemaker. In contrast, metestrus and diestrus appear unpaced, exhibiting frequent, slower activity whose loci of initiation are diffusely distributed. Our *in vivo* imaging approach also serves as a platform for potential work on uterine pathophysiology or pharmacology. In future studies, we plan to investigate the molecular mechanisms that underlie estrous-related changes and to adapt our approaches to studying the myometrium in late pregnancy.

Acknowledgements
We thank Shahinoor Begum and Andrew Preecha for technical assistance and mouse husbandry. We thank Kara McKinley and Nirao Shah for generously providing transgenic animals. We thank Ronald McCarthy for technical advice on mouse surgery and uterine tissue dissection. This work was supported by an award (D.J.C.) from Harvard Anesthesia Research Training Grant (T32, GM007592-45), the Young Investigator Award (D.J.C.) from the Society for Obstetric Anesthesiology and Perinatology, and an award (D.J.C.) from the Harvard BIRCWH Program (K12, AR084230-20).

Methods

Mouse strains and maintenance

All animal procedures adhered to the National Institutes of Health Guide for the care and use of laboratory animals and were approved by the Harvard University Institutional Animal Care and Use Committee. Progesterone Receptor (PR)-Cre$^{+/-}$ mice (JAX 017915) were generously provided by the strain's creator, Nirao Shah at Stanford University (Yang et al., 2013). Anti-Müllerian Hormone Recpetor 2 (AMHR2)-Cre+/- mice (Arango et al., 2008), were generously provided by the laboratory of Kara McKinley at Harvard University. Ai148 mice (JAX 030328), for cre-dependent GCaMP6f expression, were obtained from the Jackson Laboratory. All mice were housed in standard conditions (reverse 12-hour light/dark cycles, with water and food *ad libitum)*. For all experiments involving injection of viruses carrying *cre*-dependent payloads, genotyped female heterozygotes were generated from crosses with wild-type C57BL/6 mice obtained from Charles River Laboratories. Genotyped PR-Cre$^{+/-}$;Ai148D$^{+/-}$ or AMHR2-Cre$^{+/-}$;Ai148D$^{+/-}$ double heterozygotes were created by the crossing of respective parental strains. All genotyping was performed by Transnetyx.

Vaginal cytology and estrous cycle staging

Vaginal Cytology and estrous staging were performed by vaginal lavage with 50-100 μL of phosphate buffered saline (PBS) using a micropipette tip and suction bulb followed by crystal violet staining of freshly dried cytology preparations, as previously described (McLean et al., 2012). All cytology specimens were collected approximately 1 hour before lights-off. For virus-injected female mice, first cytology specimens were not obtained until at least 21 days post-operatively to allow for surgical recovery and restoration of uninterrupted light-dark cycling. Estrous staging was determined by daily vaginal cytology over at least five days prior to measurement. Calcium imaging of a particular estrous stage was only performed when the day-of-measurement cytology matched the cytology expected based on the prior days' specimens (see Supplemental Materials).

Virus injection surgery

AAV9 virus expressing jGCaMP8m under a CAG promoter was obtained from Addgene (162381-AAV9). For injections, pre-aliquoted frozen virus was thawed and diluted to $5x10^{12}$ GC/mL in a total volume of 10 μL, containing 10% (v/v) of trypan-blue dye to visualize spread of the injectate and to guide adjustments to the injection location(s).

For the virus injection procedure (see also Supplemental Materials), 8-12 week old heterozygous PR-Cre$^{+/-}$ female mice were anesthetized, a vertical incision was made left paramedian to the midline to access the peritoneal cavity and the left uterine horn identified. Injections were made using home-fabricated micropipettes (Sutter P1000) with beveled tips created with a home-built micropipette polisher. Micropipettes were mounted in a microinjection pump (WPI Nanoliter 2010), positioned with a micromanipulator (WPI, MP-285), and injection volumes controlled with a microsyringe pump controller (WPI, Micro4). After loading of viral injectate and positioning of the micropipette near the uterine horn, injections were performed by gentle grasping of the mesometrium with micro forceps and simultaneous advancement of the micropipette into the uterine horn. Virus was injected in two 300 nL volumes at 50 nL/sec at each injection site with 5-10 seconds of post injection time before pipette removal to assess injectate spread and prevent leakage. Injection sites consisted of 12-16 evenly spaced locations along the anterior face of the organ longitudinal axis from the left half of the uterine body (junction of the two uterine horns) to the horn end adjacent to the oviduct. Following injections, the fascial layer was closed with interrupted 5-0 monocryl sutures and the skin closed with wound clips.

Animal preparation for live animal imaging

For live animal imaging, after isoflurane anesthesia (see Supplemental Material), a midline abdominal incision was made to expose the peritoneal cavity and the bladder drained transmurally. A pair of custom 3D-printed (Anycubic, Photon Mono) semi-circular (16 mm diameter, 8 mm height) abdominal retractors were positioned at the inferior and superior borders of the abdominal incision, with extension of the incision to accommodate retractor insertion (~3.5 cm). Soaked gauze strips were adjusted to sit between the retractor and the abdominal wall to protect the wall surface from drying or damage from the retractors. The time from induction of anesthesia to collection of the last image was tracked for each animal and kept under 90 minutes. It was generally not possible to image the entirety of both uterine horns simultaneously, so for animals where both the injected and contralateral horn were imaged, gauze and retractors were adjusted to optimize the view of the imaged horn. After each animal imaging session, the animal was euthanized by isoflurane overdose followed by cervical dislocation.

Calcium imaging

The *in vivo* imaging stage was positioned below the objective of a custom optical setup for wide-field imaging previously described (Werley et al., 2017; Farhi et al., 2019). For recordings of jGCaMP8m dynamics, widefield illumination was supplied (0.1-0.2 mW mm^{-2}) with

a 470 nm LED. Excitation light was reflected off a large (65 × 80 × 3 mm) dual band (509-540 nm, 614-700 nm, Alluxa) dichroic mirror. Fluorescence was separated from back-scattered excitation by a 65 mm diameter 520/35 nm band-pass emission filter. Imaging was done via a 1X objective lens, numerical aperture 0.25 (Olympus MVPLAPO 1X). Data were captured on a Kinetix sCMOS Camera (Teledyne Photometrics) at 5 Hz framerate through a camera lens repurposed as a tube lens (VS Technology Co, VS-50085/M42). The iris was set to achieve the focal depth needed to image the convex organ surface and to accommodate any anteroposterior displacement along the organ longitudinal axis. The adjoining oviduct, junction of the two uterine horns and (often 1-2 mm) of the contralateral horn could also be imaged simultaneously. Illumination and acquisition timing was controlled using custom MATLAB software (https://www.luminosmicroscopy.com) via a National Instruments DAQ interface. For details on image processing see Supplemental Materials.

Immunostaining and confocal microscopy

For immunostaining of uterine rings (see Supplemental Materials), rings were permeabilized (0.1% Triton X-100 in PBS), blocked (1% bovine serum albumin in PBS with 0.1% Tween 20), and then incubated with the primary antibody in fresh blocking solution for 1 hr at room temperature. After secondary antibody incubation (1 hr, room temperature), rings were incubated for 5 minutes with 300 nM DAPI, washed, and mounted on glass slides. Primary antibodies were: chicken anti-GFP (Abcam, ab13970, 1:500) and rabbit anti-alpha smooth muscle actin (Abcam, ab124964, 1:500). Secondary antibodies were donkey anti-chicken Alexa Fluor 488 (Jackson Immunology 703-545-155, 1:1000) and anti-rabbit Alexa Fluor 647 (Abcam, ab150075, 1:1000).

Imaging of fixed immunostained uterine rings was performed on an LSM 700 Confocal Microscope and Zen v3.2 software (Zeiss). Image stacks were converted to maximal intensity projection images in ImageJ.

Statistics

Plots were created in MATLAB. All boxplots show median and interquartile range (IQR) with whiskers indicating 1.5 x IQR. The numbers of independent repeat experiments performed in different animals are displayed as *n* values. For statistical comparisons of features between estrous stages that proved significantly different ($p < 0.05$) by 1-way ANOVA, Tukey's test was used with a multiple comparison procedure. For paired comparison of the injected and contralateral horn, two tailed paired t-testing was performed. Sample size was determined by the practical limitations of the experiments. Researchers were not blinded.

References

Abdelaziz, M., L. Sherif, M. ElKhiary, S. Nair, S. Shalaby, S. Mohamed, N. Eziba, M. El-Lakany, D. Curiel, N. Ismail, M.P. Diamond, and A. Al-Hendy. 2016. Targeted Adenoviral Vector Demonstrates Enhanced Efficacy for In Vivo Gene Therapy of Uterine Leiomyoma. *Reprod Sci*. 23:464–474. doi:10.1177/1933719116630413.

Aguilar, H.N., and B.F. Mitchell. 2010. Physiological pathways and molecular mechanisms regulating uterine contractility. *Hum. Reprod. Update*. 16:725–744. doi:10.1093/humupd/dmq016.

Arango, N.A., A. Kobayashi, Y. Wang, S.P. Jamin, H.-H. Lee, G.D. Orvis, and R.R. Behringer. 2008. A mesenchymal perspective of Müllerian duct differentiation and regression in Amhr2-lacZ mice. *Mol Reprod Dev*. 75:1154–1162. doi:10.1002/mrd.20858.

Bertolin, K., and B.D. Murphy. 2014. 7 - Reproductive Tract Changes During the Mouse Estrous Cycle. *In* The Guide to Investigation of Mouse Pregnancy. B.A. Croy, A.T. Yamada, F.J. DeMayo, and S.L. Adamson, editors. Academic Press, Boston. 85–94.

Bulcha, J.T., Y. Wang, H. Ma, P.W.L. Tai, and G. Gao. 2021. Viral vector platforms within the gene therapy landscape. *Sig Transduct Target Ther*. 6:1–24. doi:10.1038/s41392-021-00487-6.

Bulletti, C., D. DE Ziegler, P.L. Setti, E. Cicinelli, V. Polli, and C. Flamigni. 2004. The patterns of uterine contractility in normal menstruating women: from physiology to pathology. *Ann N Y Acad Sci*. 1034:64–83. doi:10.1196/annals.1335.007.

Chamley, W.A., and H.C. Parkington. 1984. Relaxin inhibits the plateau component of the action potential in the circular myometrium of the rat. *J Physiol*. 353:51–65. doi:10.1113/jphysiol.1984.sp015321.

Crane, L.H., and L. Martin. 1991. In vivo myometrial activity in the rat during the oestrous cycle: studies with a novel technique of video laparoscopy. *Reprod Fertil Dev*. 3:185–199. doi:10.1071/rd9910185.

Dixon, R.E., S.J. Hwang, B.H. Kim, K.M. Sanders, and S.M. Ward. 2019. Myosalpinx Contractions Are Essential for Egg Transport Along the Oviduct and Are Disrupted in Reproductive Tract Diseases. *Adv Exp Med Biol*. 1124:265–294. doi:10.1007/978-981-13-5895-1_11.

Dodds, K.N., V. Staikopoulos, and E.A.H. Beckett. 2015. Uterine Contractility in the Nonpregnant Mouse: Changes During the Estrous Cycle and Effects of Chloride Channel Blockade. *Biol Reprod*. 92:141. doi:10.1095/biolreprod.115.129809.

Downing, S.J., D.G. Porter, and C.D. Redstone. 1981. Myometrial activity in rats during the oestrous cycle and pseudopregnancy: interaction of oestradiol and progesterone. *J Physiol*. 317:425–433. doi:10.1113/jphysiol.1981.sp013834.

Duquette, R.A., A. Shmygol, C. Vaillant, A. Mobasheri, M. Pope, T. Burdyga, and S. Wray. 2005. Vimentin-positive, c-kit-negative interstitial cells in human and rat uterus: a role in pacemaking? *Biol Reprod*. 72:276–283. doi:10.1095/biolreprod.104.033506.

Farhi, S.L., V.J. Parot, A. Grama, M. Yamagata, A.S. Abdelfattah, Y. Adam, S. Lou, J.J. Kim, R.E. Campbell, D.D. Cox, and A.E. Cohen. 2019. Wide-Area All-Optical Neurophysiology in Acute Brain Slices. *J. Neurosci.* 39:4889–4908. doi:10.1523/JNEUROSCI.0168-19.2019.

Griffiths, A.L., K.M. Marshall, J. Senior, C. Fleming, and D.F. Woodward. 2006. Effect of the oestrous cycle, pregnancy and uterine region on the responsiveness of the isolated mouse uterus to prostaglandin F(2alpha) and the thromboxane mimetic U46619. *J Endocrinol*. 188:569–577. doi:10.1677/joe.1.06466.

Hou, J.H., J.M. Kralj, A.D. Douglass, F. Engert, and A.E. Cohen. 2014. Simultaneous mapping of membrane voltage and calcium in zebrafish heart in vivo reveals chamber-specific developmental transitions in ionic currents. *Front. Physiol.* 5:344. doi:10/gffj2b.

Ishikawa, M., and A.R. Fuchs. 1978. Electrical and mechanical activity of rat uterus in vivo during the estrous cycle. *Am. J. Obstet. Gynecol.* 132:611–619. doi:10.1016/0002-9378(78)90852-9.

Jakobs, M.A.H., A. Dimitracopoulos, and K. Franze. 2019. KymoButler, a deep learning software for automated kymograph analysis. *Elife*. 8:e42288. doi:10.7554/eLife.42288.

Jia, B.Z., Y. Qi, J.D. Wong-Campos, S.G. Megason, and A.E. Cohen. 2023. A bioelectrical phase transition patterns the first vertebrate heartbeats. *Nature*. 622:149–155. doi:10.1038/s41586-023-06561-z.

Kawarabayashi, T., and T. Osa. 1976. Comparative investigations of alpha- and beta-effects on the longitudinal and circular muscles of the pregnant rat myometrium. *Jpn J Physiol*. 26:403–416. doi:10.2170/jjphysiol.26.403.

Kunz, G., and G. Leyendecker. 2002. Uterine peristaltic activity during the menstrual cycle: characterization, regulation, function and dysfunction. *Reprod Biomed Online*. 4 Suppl 3:5–9. doi:10.1016/s1472-6483(12)60108-4.

Lammers, W.J.E.P. 2013. The electrical activities of the uterus during pregnancy. *Reprod Sci*. 20:182–189. doi:10.1177/1933719112446082.

Lutton, E.J., W.J.E.P. Lammers, S. James, H.A. van den Berg, and A.M. Blanks. 2018. Identification of uterine pacemaker regions at the myometrial-placental interface in the rat. *J. Physiol. (Lond.)*. 596:2841–2852. doi:10.1113/JP275688.

Ma, X., P. Zhao, M. Wakle-Prabagaran, C. Amazu, M. Malik, W. Wu, H. Wang, Y. Wang, and S.K. England. 2020. Microelectrode array analysis of mouse uterine smooth muscle electrical activity†. *Biol Reprod*. 102:935–942. doi:10.1093/biolre/ioz214.

Malik, M., M. Roh, and S.K. England. 2021. Uterine contractions in rodent models and humans. *Acta Physiol (Oxf)*. 231:e13607. doi:10.1111/apha.13607.

McCloskey, C., C. Rada, E. Bailey, S. McCavera, H.A. van den Berg, J. Atia, D.A. Rand, A. Shmygol, Y.-W. Chan, S. Quenby, J.J. Brosens, M. Vatish, J. Zhang, J.S. Denton, M.J. Taggart, C. Kettleborough, D. Tickle, J. Jerman, P. Wright, T. Dale, S. Kanumilli, D.J. Trezise, S. Thornton, P. Brown, R. Catalano, N. Lin, S.K. England, and A.M. Blanks. 2014. The inwardly rectifying K+ channel KIR7.1 controls uterine excitability throughout pregnancy. *EMBO Mol Med*. 6:1161–1174. doi:10.15252/emmm.201403944.

McLean, A.C., N. Valenzuela, S. Fai, and S.A.L. Bennett. 2012. Performing vaginal lavage, crystal violet staining, and vaginal cytological evaluation for mouse estrous cycle staging identification. *J Vis Exp*. e4389. doi:10.3791/4389.

Mucenski, M.L., R. Mahoney, M. Adam, A.S. Potter, and S.S. Potter. 2019. Single cell RNA-seq study of wild type and Hox9,10,11 mutant developing uterus. *Sci Rep*. 9:4557. doi:10.1038/s41598-019-40923-w.

Ren, C., and T. Komiyama. 2021. Characterizing Cortex-Wide Dynamics with Wide-Field Calcium Imaging. *J Neurosci*. 41:4160–4168. doi:10.1523/JNEUROSCI.3003-20.2021.

Rendt, J.M., L. Toro, E. Stefani, and S.D. Erulkar. 1992. Progesterone increases Ca2+ currents in myometrial cells from immature and nonpregnant adult rats. *Am J Physiol*. 262:C293-301. doi:10.1152/ajpcell.1992.262.2.C293.

Ruckebusch, Y., and F. Bayard. 1975. Motility of the oviduct and uterus of the cow during the oestrous cycle. *J Reprod Fertil*. 43:23–32. doi:10.1530/jrf.0.0430023.

Sanchez, C., C. Berthier, Y. Tourneur, L. Monteiro, B. Allard, L. Csernoch, and V. Jacquemond. 2021. Detection of Ca2+ transients near ryanodine receptors by targeting fluorescent Ca2+ sensors to the triad. *J Gen Physiol*. 153:e202012592. doi:10.1085/jgp.202012592.

Sheldon, R.E., A. Shmygol, H.A. Van Den Berg, and A.M. Blanks. 2015. Functional and Morphological Development of the Womb Throughout Life. *Science Progress*. 98:103–127. doi:10.3184/003685015X14308363103415.

Soyal, S.M., A. Mukherjee, K.Y.-S. Lee, J. Li, H. Li, F.J. DeMayo, and J.P. Lydon. 2005. Cre-mediated recombination in cell lineages that express the progesterone receptor. *Genesis*. 41:58–66. doi:10.1002/gene.20098.

Steinmetz, N.A., C. Buetfering, J. Lecoq, C.R. Lee, A.J. Peters, E.A.K. Jacobs, P. Coen, D.R. Ollerenshaw, M.T. Valley, S.E.J. de Vries, M. Garrett, J. Zhuang, P.A. Groblewski, S. Manavi, J. Miles, C. White, E. Lee, F. Griffin, J.D. Larkin, K. Roll, S. Cross, T.V. Nguyen, R. Larsen, J. Pendergraft, T. Daigle, B. Tasic, C.L. Thompson, J. Waters, S. Olsen, D.J. Margolis, H. Zeng, M. Hausser, M. Carandini, and K.D. Harris. 2017. Aberrant Cortical Activity in Multiple

GCaMP6-Expressing Transgenic Mouse Lines. *eNeuro*. 4. doi:10.1523/ENEURO.0207-17.2017.

Stevenson, A.J., G. Vanwalleghem, T.A. Stewart, N.D. Condon, B. Lloyd-Lewis, N. Marino, J.W. Putney, E.K. Scott, A.D. Ewing, and F.M. Davis. 2020. Multiscale imaging of basal cell dynamics in the functionally mature mammary gland. *Proc Natl Acad Sci U S A*. 117:26822–26832. doi:10.1073/pnas.2016905117.

Talo, A., and A.E. Kärki. 1976. Electric activity of the rat myometrium in vivo during the estrous cycle. *Acta Physiol Scand*. 97:495–500. doi:10.1111/j.1748-1716.1976.tb10289.x.

Thilander, G., G.J. King, and R.E. Garfield. 1993. Connexin43 and gap junction content in the porcine myometrium during the estrous cycle. *Theriogenology*. 40:323–332. doi:10.1016/0093-691x(93)90270-f.

Toro, L., E. Stefani, and S. Erulkar. 1990. Hormonal regulation of potassium currents in single myometrial cells. *Proc Natl Acad Sci U S A*. 87:2892–2895. doi:10.1073/pnas.87.8.2892.

Wang, H., and S.K. Dey. 2006. Roadmap to embryo implantation: clues from mouse models. *Nat Rev Genet*. 7:185–199. doi:10.1038/nrg1808.

Wang, S., K. Anderson, S. Pizzella, H. Xu, Z. Wen, Y. Lin, Y. Nan, J. Lau, Q. Wang, V. Ratts, and Y. Wang. 2023. Noninvasive electrophysiological imaging identifies 4D uterine peristalsis patterns in subjects with normal menstrual cycles and patients with endometriosis. *Res Sq*. rs.3.rs-2432192. doi:10.21203/rs.3.rs-2432192/v1.

Weinmann, J., S. Weis, J. Sippel, W. Tulalamba, A. Remes, J. El Andari, A.-K. Herrmann, Q.H. Pham, C. Borowski, S. Hille, T. Schönberger, N. Frey, M. Lenter, T. VandenDriessche, O.J. Müller, M.K. Chuah, T. Lamla, and D. Grimm. 2020. Identification of a myotropic AAV by massively parallel in vivo evaluation of barcoded capsid variants. *Nat Commun*. 11:5432. doi:10.1038/s41467-020-19230-w.

Werley, C.A., M.-P. Chien, and A.E. Cohen. 2017. Ultrawidefield microscope for high-speed fluorescence imaging and targeted optogenetic stimulation. *Biomedical optics express*. 8:5794–5813. doi:10/gg83rc.

Wheaton, L.G., G.J. Pijanowski, P.G. Weston, and T.J. Burke. 1988. Uterine motility during the estrous cycle: studies in healthy bitches. *Am J Vet Res*. 49:82–86.

Wray, S., and S. Arrowsmith. 2021. Uterine Excitability and Ion Channels and Their Changes with Gestation and Hormonal Environment. *Annu Rev Physiol*. 83:331–357. doi:10.1146/annurev-physiol-032420-035509.

Wray, S., and K. Noble. 2008. Sex hormones and excitation-contraction coupling in the uterus: the effects of oestrous and hormones. *J. Neuroendocrinol.* 20:451–461. doi:10.1111/j.1365-2826.2008.01665.x.

Yang, C.F., M.C. Chiang, D.C. Gray, M. Prabhakaran, M. Alvarado, S.A. Juntti, E.K. Unger, J.A. Wells, and N.M. Shah. 2013. Sexually dimorphic neurons in the ventromedial hypothalamus govern mating in both sexes and aggression in males. *Cell*. 153:896–909. doi:10.1016/j.cell.2013.04.017.

Young, R.C. 2016. Mechanotransduction mechanisms for coordinating uterine contractions in human labor. *Reproduction*. 152:R51-61. doi:10.1530/REP-16-0156.

Young, R.C. 2018. The uterine pacemaker of labor. *Best Pract Res Clin Obstet Gynaecol*. 52:68–87. doi:10.1016/j.bpobgyn.2018.04.002.

Zenclussen, A.C., D.N. Olivieri, M.L. Dustin, and C.E. Tadokoro. 2013. In vivo multiphoton microscopy technique to reveal the physiology of the mouse uterus. *Am. J. Reprod. Immunol.* 69:281–289. doi:10.1111/aji.12066.

Zhang, Y., J. Qian, O. Zaltzhendler, M. Bshara, A.J. Jaffa, D. Grisaru, E. Duan, and D. Elad. 2019. Analysis of in vivo uterine peristalsis in the non-pregnant female mouse. *Interface Focus*. 9:20180082. doi:10.1098/rsfs.2018.0082.

Zhang, Y., M. Rózsa, Y. Liang, D. Bushey, Z. Wei, J. Zheng, D. Reep, G.J. Broussard, A. Tsang, G. Tsegaye, S. Narayan, C.J. Obara, J.-X. Lim, R. Patel, R. Zhang, M.B. Ahrens, G.C. Turner, S.S.-H. Wang, W.L. Korff, E.R. Schreiter, K. Svoboda, J.P. Hasseman, I. Kolb, and L.L. Looger. 2023. Fast and sensitive GCaMP calcium indicators for imaging neural populations. *Nature*. 615:884–891. doi:10.1038/s41586-023-05828-9.

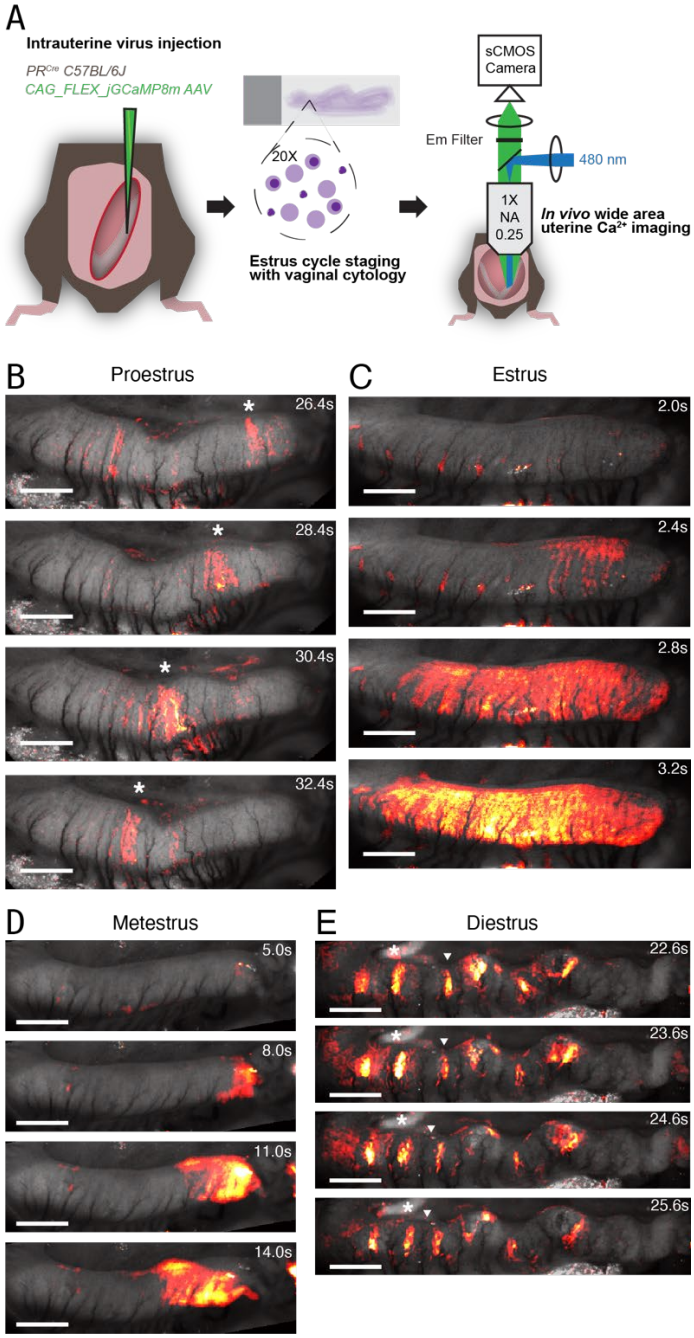

Figure 1: Live animal wide-area uterine calcium imaging during estrous cycle. (A) Experimental scheme. Left panel: The uterus was injected with AAV virus encoding GCaMP8m. Middle: Estrous stage was determined with vaginal cytology. Right: Uterine calcium dynamics were imaged on an ultra-widefield microscope. Images from movies of calcium dynamics with the change in fluorescence in color overlaid on a grayscale image of the basal fluorescence for (B) proestrus, (C) estrus, (D) metestrus, and (E) diestrus. Asterisks (B and E) and arrowheads (E) mark propagating bands of activity in successive images. Scale bars 1 mm in all images.

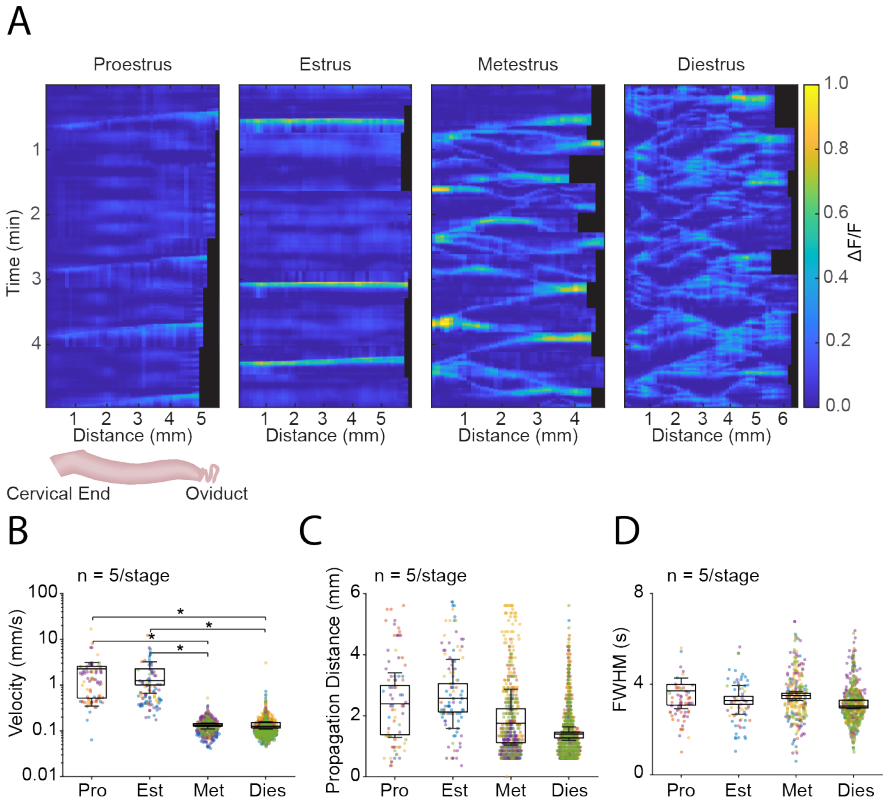

Figure 2: Uterine calcium dynamics vary by estrous stage. (A) Representative kymographs of fold-change in fluorescence for each estrous stage. For each panel, the right-most spatial coordinate is closest to the oviduct. Black regions indicate organ length contractions, leading to no data from the ovarian end. Event-wise distributions of (B) propagation velocity, (C) distance and (D) full width at half maximum (FWHM). Box plots represent IQR (25th, 50th, and 75th percentile) with whiskers representing 1.5 × IQR. Swarm plot points represent values from individual calcium events. Colors identify events occurring in the same animal. Proestrus (Pro), estrus (Est), metestrus (Met) and diestrus (Dies) stages had n = 5 animals per stage. For statistics (B), $P < 0.01$ (1 way ANOVA), with multiple-comparisons testing by Tukey's test where *$P < 0.05$.

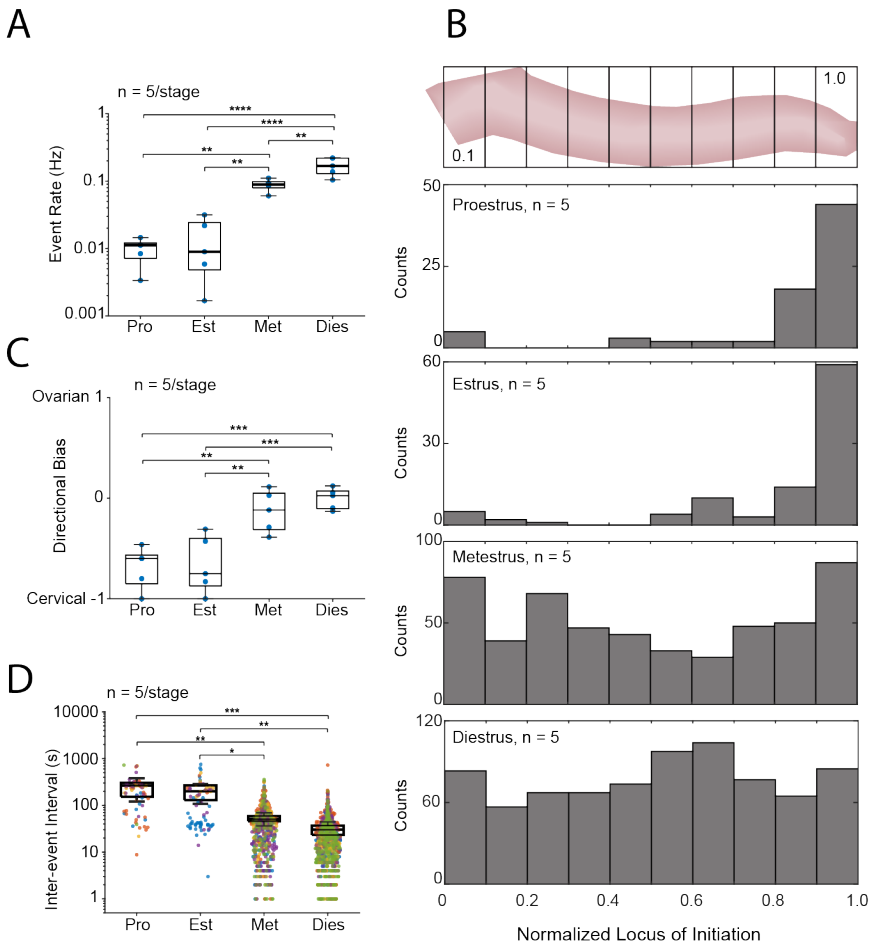

Figure 3: Frequency, direction, and loci of initiation of uterine calcium events vary by estrous stage. Distributions of (A) event rate, (C) directional bias, and (D) inter-event interval. (B) Histograms of event loci of initiation, normalized relative to uterine horn length and binned into deciles as indicated in the top panel. Counts represent all events across 5 animals per stage. Box plots represent IQR (25th, 50th, and 75th percentile) with whiskers representing 1.5 $\times$ IQR. Data points (A and C) represent individual animals or pairs of successive calcium events (D). Colored points in swarm plot (D) identify events occurring in the same animal. Proestrus (Pro), estrus (Est), metestrus (Met) and diestrus (Dies) stages had n = 5 animals per stage. For statistics, $P < 1 \times 10^{-6}$ (B), $P < 1 \times 10^{-4}$ (C), and $P < 0.002$ (D) by 1 way ANOVA; multiple-comparisons testing by Tukey's test where *P < 0.05, **P < 0.01, ***P < 0.001, ****$P < 1 \times 10^{-4}$.

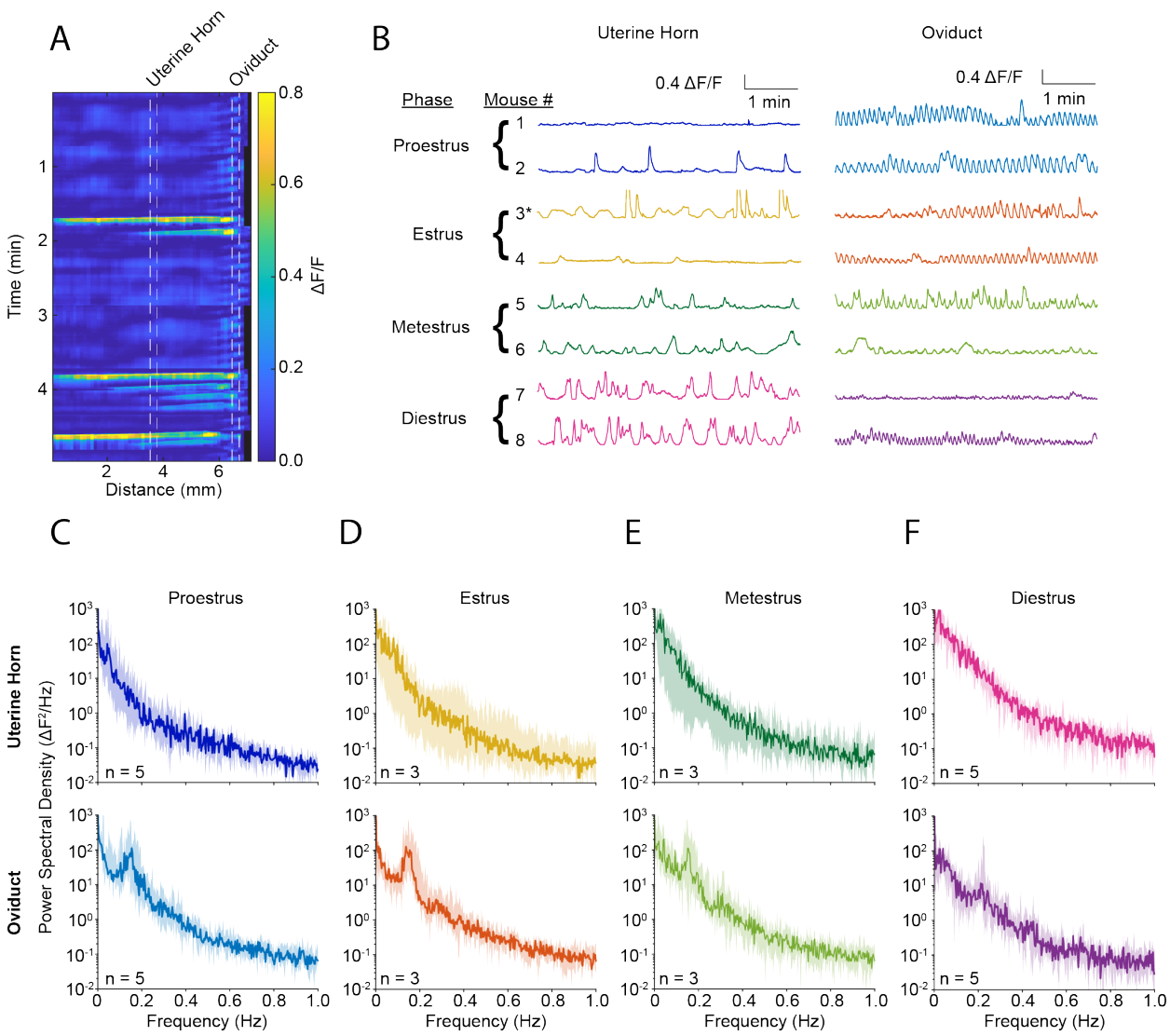

Figure 4: Uterine calcium dynamics are not periodic. (A) Kymograph with overlaid marks indicating regions analyzed for uterine horn and oviduct. (B) Representative fluorescence traces from two mice in each estrous stage. Asterisks indicate traces derived from the kymograph in (A). (C-F) Power spectral density of the uterine horn (top panels) and oviduct (lower panels) for each stage of estrous. The number of animals is marked on each panel.